Chemical Engineering Journal 433 (2022) 134568

Contents lists available at ScienceDirect

Chemical Engineering Journal

journal homepage: www.elsevier.com/locate/cej

Optimization of bioinspired surfaces with enhanced water transportation capacity

Ziai Liu [a,b], Hang Liu [c], Wei Li [b], Jinlong Song [a,*]

[a] Key Laboratory for Precision and Non-traditional Machining Technology of the Ministry of Education, Dalian University of Technology, Dalian 116024, PR China
[b] GPL Photonics Laboratory, State Key Laboratory of Applied Optics, Changchun Institute of Optics, Fine Mechanics and Physics, Chinese Academy of Sciences, Changchun 130033, PR China
[c] Department of In Vitro Diagnosis, Mindray Bio-Medical Electronics Co., Ltd, Shenzhen 518000, PR China

ARTICLE INFO

Keywords:
Bioinspired surface
Super-wettability
Serial-wedge-shaped channel
Water transportation
Numerical simulation

ABSTRACT

Spontaneous and directional pumpless transportation (SDPT) of water on engineering surfaces that mimics the dorsal integument of *Phrynosoma cornutum* has promising applications in water harvesting platforms, heat transfer equipment, *etc.*, yet is limited owing to the expensive processing techniques, complicated preparing processes, and poor transportation capacities. Herein, a facile approach is developed to fabricate the patterned super-wettability surfaces with superhydrophilic serial-wedge-shaped channels embedded in superhydrophobic panels. The SDPT of water actuated by a Laplace pressure difference can be achieved conveniently on the serial-wedge-shaped channels. Furthermore, the transportation capacities of the channels with different configuration parameters are explored by numerical simulation and experimental verification simultaneously in this study. In addition, by taking advantage of an optimization strategy, the optimized channels with the improved configurations are developed, which can not only enhance the scale of configuration parameters engendering the continuous SDPT but can also enhance the transportation velocity of water. The present study will provide important insights into the design of next-generation high-performance fluid transportation systems.

1. Introduction

Water transportation is ubiquitous in nature [1–3] and is also highly desired in a wide spectrum of technical systems ranging from fog collection [4], inkjet printing [5], membrane filtration [6–8], and biomedical testing [9], to hydropower generation [10–12]. Numerous natural species are capable of realizing spontaneous and directional pumpless transportation (SDPT) of water by controlling the interaction between their micro/nano surface structures with water [1–3,13,14]. For instance, the Texas horned lizard *Phrynosoma cornutum* inhabiting arid regions of North America utilizes its highly-evolved dorsal integument to collect dew and transport water to its snout where water is ingested [3,15]. In more detail, the integument of *P. cornutum* consists of upper microsized overlapping scales showing water repellency (hydrophobicity) and lower nanosized geometry-gradient capillary channels showing water affinity (hydrophilicity) [16]. Such hierarchical structures with diverse wettability can direct water in a pre-determined flow direction without external energy input [17–19]. It has to be emphasized that the self-driven transportation of *P. cornutum* is based on geometric principles and mainly actuated by a *Laplace* pressure difference which is generated owing to the configuration of channels [20,21]. Comanns *et al.* observed that a single geometry-gradient capillary channel on the dorsal integument of *P. cornutum* is composed of several wedge-shaped grooves with different sizes and any two adjacent channels are interconnected, forming a capillary network [3,16].

Over the past decades, scientists and engineers have been fascinated by the sophisticated structures and the intriguing transportation phenomenon of *P. cornutum*'s dorsal integument. By mimicking such a natural surface, a variety of bioinspired surfaces showing extreme water repellency and water affinity (referred to as superhydrophobicity and superhydrophilicity, respectively) that can realize the SDPT of water have been demonstrated. Meanwhile, researchers found that there are two principles should be based for the fabrication of such surfaces: (I) a patterned super-wettability surface (PSS) with a superhydrophilic channel embedded in a superhydrophobic panel should be prepared. (II) the superhydrophilic channel should possess a geometry gradient. When a water droplet is dispensed on the narrow side of a superhydrophilic geometry-gradient channel of a PSS, it will be immediately captured and

* Corresponding author.
E-mail address: songjinlong@dlut.edu.cn (J. Song).

https://doi.org/10.1016/j.cej.2022.134568
Received 28 October 2021; Received in revised form 21 December 2021; Accepted 4 January 2022
Available online 7 January 2022

then squeezed along the channel to the wide side, generating a *Laplace* pressure difference between the front and backside of the droplet and resulting in its continuous transportation. Li *et al.* classified the SDPT of water on PSSs as spreading transportation, in which case water just propagates in one direction but pins in all others [22]. Although the SDPT of water has been successfully demonstrated on PSSs with superhydrophilic wedge-like (wedge-shaped, teardrop-shaped, root-shaped, vein-shaped, et al.) channels [23–26], it still suffers from the defects including overmuch mass loss on channels owing to spreading transportation [27], limited water transportation velocity, or high costs for preparing the PSSs with delicate structures [28,29]. Specifically, for a wedge-like channel with a certain wedge angle but an uncertain length, its wide side width is proportional to length, indicating that water will spread along both the length direction and the width direction of the channel, which further means that water flow direction cannot be well regulated and the efficiency of SDPT will be low. In addition, the configuration of the wedge-like channel will accelerate the decrease of apparent contact angles difference during SDPT, and therefore leads to the sharp decrease of inner *Laplace* pressure difference which mainly drives the spontaneous process. As a result, water transportation velocity on the wedge-like channel at a long distance will be significantly reduced because the inner *Laplace* pressure difference will be insufficient.

Instead, a PSS with a serial-wedge-shaped channel which is composed of several identical single wedge-shaped channels connecting in a head-to-tail arrangement was proposed to realize the long-distance SDPT of subaqueous bubbles in our prior study [27]. Different from conventional wedge-like channels, the wide side width of the serial-wedge-shaped channel is independent of length, which is beneficial to reduce the mass loss caused by spreading transportation because water is mainly transported along the length direction. Compared with the transportation on the wedge-like channel, the apparent contact angles difference during SDPT can be well maintained. Therefore, a sufficient inner *Laplace* pressure difference as well as a high transportation velocity can be guaranteed for long-distance SDPT. Additionally, the research on geometry-gradient channels with periodic and asymmetrical structures for SDPT of water has blossomed over the past five years. For instance, Hou *et al* fabricated superhydrophilic serial-wedge-shaped channels on a superhydrophobic panel and then realized the SDPT of water with the assistance of gravity [30]. Wang *et al.* prepared an integrating platform with a hydrophilic bamboo-joint-like channel through 3D printing technique and achieved the long-distance SDPT of water to a target area [31]. Shi *et al.* found that a hydrophilic ladder-like tapered pillar processed by electrochemical etching could realize the anti-gravity and long-distance SDPT of water from the pillar tip to the base end [32]. Similarly, Feng *et al.* exploited a hydrophilic integrating tapered pillar with both geometry gradient and wetting gradient by using electrochemical etching and anodic oxidation, which was also capable of spontaneously and directionally transporting water for a long distance [33]. Significant progress has been achieved on the long-distance SDPT of water; however, the transportation capacities of the existing geometry-gradient channels/structures are far from satisfactory, which also hamper their further practical applications. Therefore, proposing an effective strategy for optimization of the geometry-gradient channels/structures' configurations to enhance their water transportation capacities is of vital importance.

Herein, we utilized two-step nanosecond laser ablation and low surface energy materials modification to efficiently fabricate a bio-inspired PSS with a superhydrophilic serial-wedge-shaped channel embedded in a superhydrophobic panel, which is based on the inspiration of *P. cornutum*'s dorsal integument and our prior study. Water droplets can bead up with $\sim 157^{\circ}$ contact angle on the superhydrophobic panel while spread completely with $\sim 0^{\circ}$ contact angle on the superhydrophilic channel. Meanwhile, the SDPT of water propelled by a *Laplace* pressure difference can be achieved on the serial-wedge-shaped channel owing to its geometry gradient. To better understand the transportation capacity of the channel, a systemical investigation consisting of numerical simulation and experimental verification is employed. Furthermore, by taking advantage of an optimization strategy, the original serial-wedge-shaped channel can be adjusted from an angular configuration to a smooth configuration, which is expected to improve droplet motion status at the junction and also enhance transportation velocity. We envision that our study may provide more possibilities for the development of water harvesting platforms and heat transfer equipment, and will also open up new avenues for next-generation high-performance fluid transportation systems.

2. Experimental section

2.1. Sample preparation

Fabrication of a homogeneous superhydrophobic surface: The aluminum (Al) sheet (100 mm × 30 mm × 2 mm) with 99.9 % purity was first cleaned ultrasonically in absolute ethanol for 5 min to remove impurities. After drying in air, the Al sheet was subjected to a laser-ablation process by a nanosecond laser system (SK-CX30, Sanke) that can generate a center wavelength of 1064 nm nanosecond laser to construct hierarchical rough microstructures. The repetition rate of 20 kHz and the optical focus diameter of 50 μm were held constant during the process. The laser power of 24 W and the scanning speed of 500 $mm \cdot s^{-1}$ were utilized to prepare a homogeneous superhydrophilic surface on the Al sheet. To render the surface superhydrophobic, the laser-ablated surface was subsequently dipped into 1 wt% fluoroalkyl silane (FAS, $C_8F_{13}H_4Si(OCH_2CH_3)_3$, Degussa) ethanol solution for 30 min, followed by drying at 60 °C for 10 min.

Fabrication of a patterned super-wettability surface: The homogeneous superhydrophobic surface was resubjected to the laser-ablation process to prepare superhydrophilic channels with designed configurations at the laser power of 12 W and the scanning speed of 1000 $mm \cdot s^{-1}$ (The decreased laser power and the increased scanning speed were adopted to reduce the influence of laser on the unprocessed superhydrophobic region); wherein, the motion path of the laser beam was regulated by a computer.

2.2. Characterization

Micromorphology and 3D profile of the obtained surfaces were observed by a field-emission scanning electron microscope (FE-SEM, FEI NOVA NanoSEM 450) and an optical profilometer (VR-3000, Keyence). Elements and crystal structures were characterized using energy dispersive spectroscopy (EDS, INCA Energy) and X-ray diffraction (XRD-6000, Empyrean), respectively. The X-ray source was a Co Kα radiation, with $\lambda = 0.1789010$ nm, a scan rate of 0.039 $deg \cdot min^{-1}$, a 2θ range of $30^{\circ} \sim 130^{\circ}$. Static contact angles were measured by an optical goniometer (Krüss, DSA100) using 5 μL droplets, which were based on 5 measurements obtained at different positions. The volume of droplets used in transportation processes was 40 μL and the droplets were released onto the PSSs by a dropwise dispensing system (LSP02-2A, LongerPump) as shown in Fig. S1. Digital images were taken using an SLR camera (D7200, Nikon) equipped with a 105 mm lens.

2.3. Numerical simulation

The geometric model of Al sheet with a PSS was developed in Pro/E software and was subsequently exported to ICEM CFD to generate computational grids. The meshing element used in ICEM CFD for meshing the whole domain was the tetrahedral element. Simulation of the SDPT of a droplet on a PSS was performed using the commercial software ANSYS Fluent, and the simulation result data was exported with CFD-Post. During the simulation process, a droplet of radius 2.12 mm (∼40 μL) was initially static near the narrow side of the serial-wedge-shaped channel and the contact angles of the superhydrophilic and superhydrophobic regions were 0° and 160°, respectively. Moreover, the calculation time step was set as $\Delta t = 5 \times 10^{-5}$ s to obtain precise results and efficient calculations.

3. Results and discussion

Fig. 1(a) shows the digital image of the as-prepared PSS, consisting of several superhydrophilic serial-wedge-shaped channels embedded in a superhydrophobic panel; static contact angles of 5 μL droplet on the superhydrophilic and superhydrophobic regions are 0° and 157 ± 2°, respectively. After the dyed droplets were dispensed at the narrow side of the channels, water easily wet the serial-wedge-shaped channels without leaving any traces on the panel. As the schematic depicted in Fig. 1(b), the configuration of a serial-wedge-shaped channel is composed of periodic identical wedges and presents the head-to-tail linkages; wherein the connection area between every-two wedges is referred to as the junction. Moreover, the 3D profile image of the junction and the cross-section schematic of the channel are shown in Fig. 1(c) and Fig. 1(d), respectively, which demonstrate that the hierarchical rough microstructures of the channel consist of evenly arranged cones with the height of ∼ 50 μm. It is thus clear that the height difference between the channel bottom and the panel is ∼ 50 μm, which is also the depth of the channel. Fig. 1(e) shows the schematic of the dorsal integument of *P. cornutum* which processes the hierarchical structures with superhydrophilicity and superhydrophobicity [3]. It can be observed that the features of our bioinspired PSS including configuration and wettability are similar to those of *P. cornutum*. SEM images of the micron-sized cones are shown in Fig. 1(f) and (g), revealing the presence of irregular scaly particles with the size of a few hundreds of nanometers to a few microns. These particles were produced on account of the melting and solidification of Al during laser ablation. Additionally, a similar morphology can also be observed on the superhydrophobic panel as shown in Fig. S2. Although the channel and the panel are ablated under different laser parameters, there are no significant differences between the sizes of microstructures of these two regions.

XRD patterns of different regions of a PSS are demonstrated in Fig. S3 (a) and the diffraction peaks manifest that the main compositions of both the superhydrophobic panel and the superhydrophilic channel are Al and Al_2O_3. As the EDS spectra shown in Fig. S3(b), absorption bands assigned to the elements of C, O, F, Al, and Si are detected on the superhydrophobic panel, which demonstrate that the low surface energy groups of Si-O-Si and C-F belong to FAS are successfully assembled on the surface [34]. In contrast, the elements of F and Si are missing on the superhydrophilic channel (Fig. S3(c)), which verifies that the FAS layer has already been removed.

As shown in Fig. 2(a) and (b), for a serial-wedge-shaped channel with a certain wedge angle α, the channel configuration is regulated by two independent parameters: the narrow width of the junction w_1 and the wide width of the junction w_2. It is necessary to note that w_2 is also the wide side width of the channel. Herein, we first identified the transportation capacity of the serial-wedge-shaped channels by transporting droplets on the channels with α of 4°, w_2 of 2.0 mm, and diverse w_1. Droplets were dispensed at the starting points (left) of the channels placed horizontally. As shown in the top images of Fig. 2(c) and (d), once the droplets were captured by the first wedge of the channels, the droplets were elongated in the lateral direction toward the terminal points (right) of the channels. Meanwhile, the droplets were separated into an anterior front and a posterior bulge in the first 50 ms. Capillary imbibition causes the fast-flowing of the front, while the difference between the tail radius R_t and the head radius R_h of the bulge generates inner Laplace pressure difference ΔP for the driving force (Laplace force F_L), which can be expressed as follows

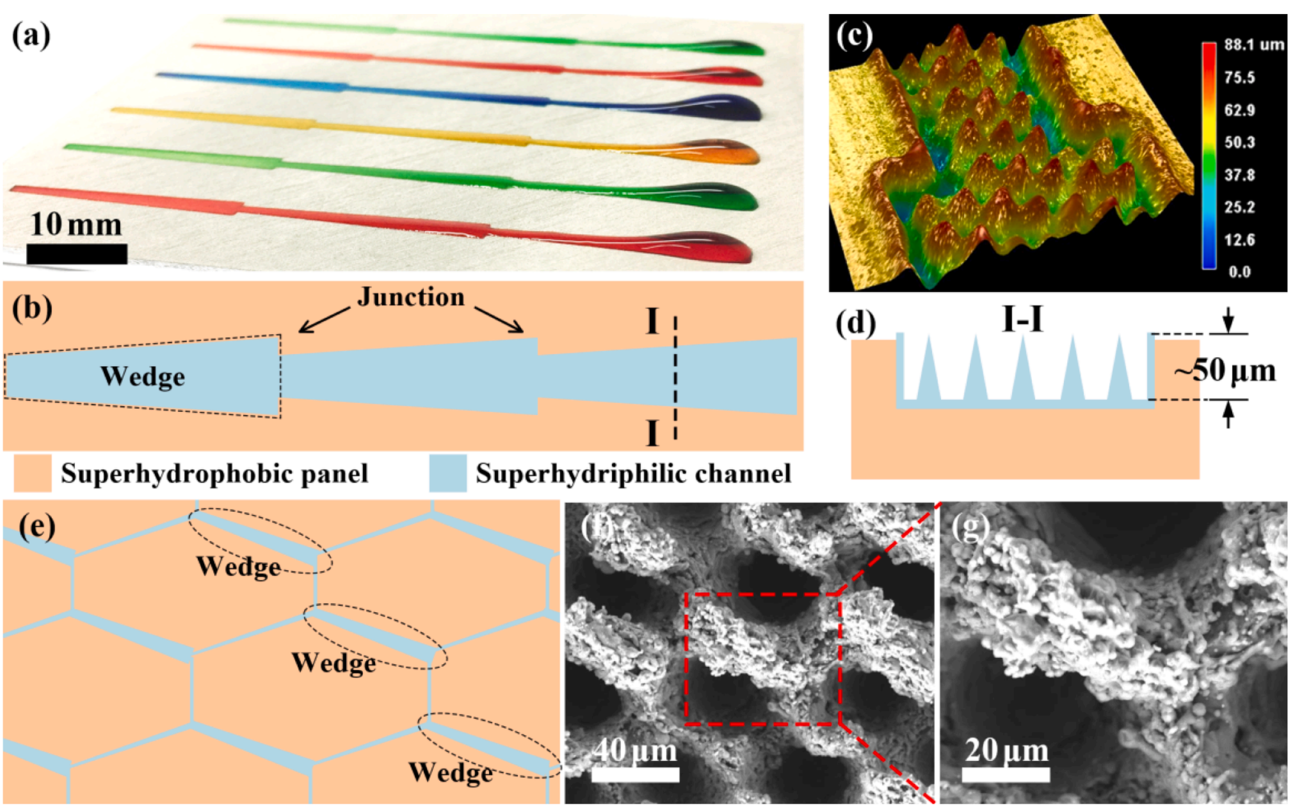

Fig. 1. Characterization and schematics of the PSS. (a) Digital image of the PSS with dyed water. (b) Schematic of a PSS. (c) 3D profile image of the junction. (d) Cross-section schematic of a serial-wedge-shaped channel. (e) Schematic of the dorsal integument of *P. cornutum* [3]. (f, g) SEM images of the superhydrophilic channel under different magnifications.

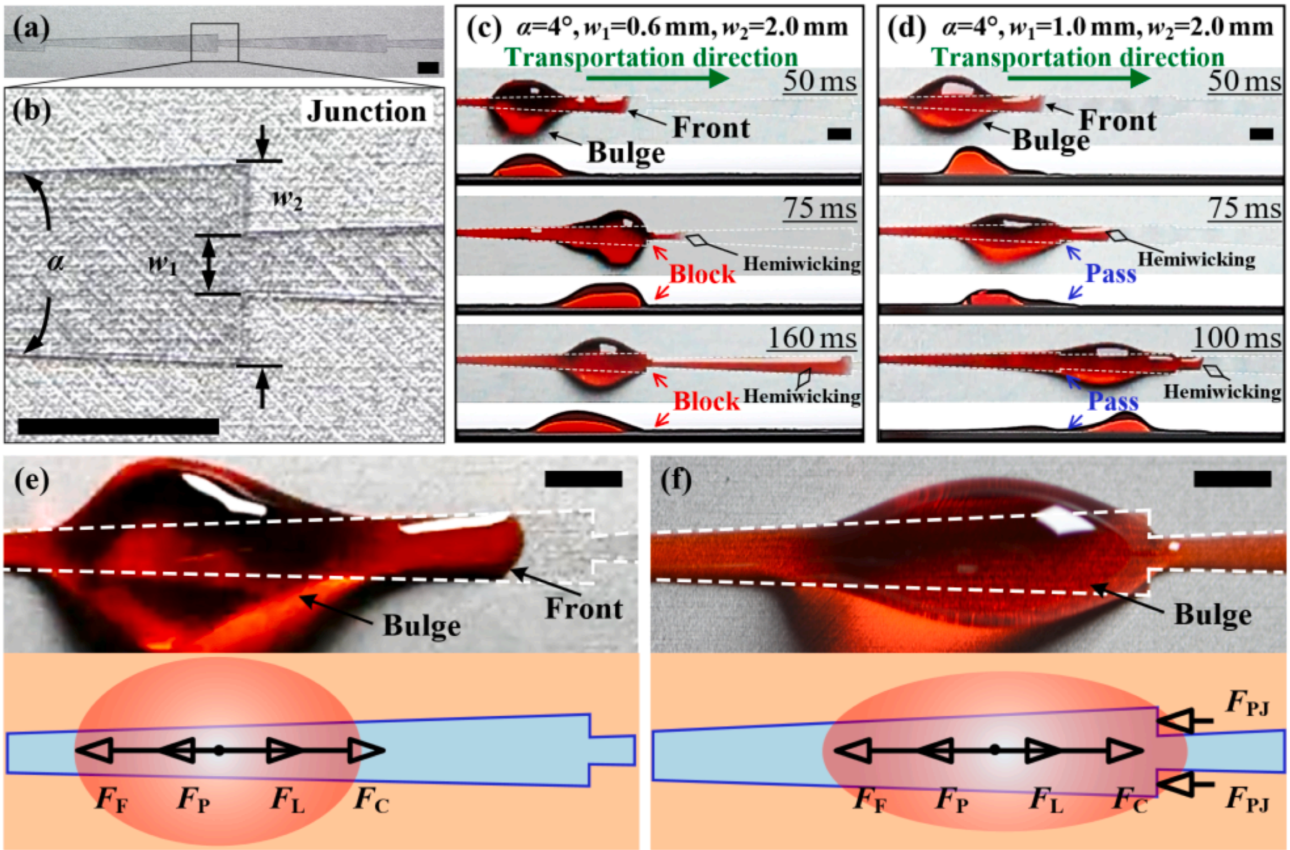

Fig. 2. SDPT of droplets on the PSSs. (a) Digital image of a PSS. (b) A close-up image of a junction. (c) Transportation processes on the serial-wedge-shaped channel with $\alpha = 4^\circ$, $w_1 = 0.6$ mm, $w_2 = 2.0$ mm showing the block-status. (d) Transportation processes on the serial-wedge-shaped channel with $\alpha = 4^\circ$, $w_1 = 1.0$ mm, $w_2 = 2.0$ mm showing the pass-status. (e) Force analysis of the droplet on the first wedge of the channel. (f) Force analysis of the droplet arriving at the first junction of the channel. Scale bars, (a ~ f): 2.0 mm.

$$F_L \approx \Delta P \approx 2\gamma_1 \left(\frac{1}{R_t} - \frac{1}{R_h}\right) \tag{1}$$

where γ_1 is the surface tension of the interface between water and air.

As can be seen, despite the motions of droplets were similar in the initial stage of 0 ms ~ 50 ms, distinct transportation phenomena were subsequently visualized on the serial-wedge-shaped channels with diverse w_1. Fig. 2(c) shows that the droplet could not be transported continuously on the channel with $w_1 = 0.6$ mm; although the anterior front crossed the first junction at 75 ms owing to hemiwicking, the posterior bulge was still blocked at the junction, resulting in the unsuccessful SDPT. On the contrary, for the channel with $w_1 = 1.0$ mm, both the front and the bulge passed the first junction of the channel as shown in Fig. 2(d), achieving the continuous SDPT.

We then qualitatively analyzed the underlying mechanism of the SDPT of a droplet on the serial-wedge-shaped channel and the reason for droplets showing two distinct motion statuses (block-status and pass-status) at the first junctions with diverse w_1. Fig. 2(e) illustrates the forces acting on the droplet during its transportation on the first wedge of the channel, including capillary force F_C, Laplace force F_L, pinning force F_P, and frictional force F_F. Thereinto, F_C and F_L are the driving forces, while F_P and F_F are the opposing forces. The resultant force F can be deduced by the following equation [35].

$$F = F_C + F_L + F_P + F_F \tag{2}$$

Thereinto, F_L is the main driving force that triggers the SDPT; F_C originates from the multiscale rough microstructures of the channel surface and causes the hemiwicking phenomenon promoting the movement of the front; F_P is the opposing force acting on the boundary line of the front of the droplet impeding transportation; F_F is the internal friction of water during transportation. The equations and the corresponding influence factors of F_C, F_P, and F_F are shown in Fig. S4.

Once the elongated droplet arrives at the first junction as shown in Fig. 2(f), the SDPT will be hindered by the lengthwise boundary of the junction, which is perpendicular to the transportation direction. By this time, a new pinning force from the junction will be generated, which is referred to as F_{PJ}. According to the observations illustrated in Fig. 2(c) and (d), for a serial-wedge-shaped channel with a certain α and a certain w_2, if the channel has a smaller w_1, the junction will possess a longer lengthwise boundary (w_2-w_1); when a droplet is transported to the first junction of such a channel during the SDPT, the pinning effect at the junction will be more obvious and the larger F_{PJ} produced by the lengthwise boundary of the junction may cease the SDPT.

The two transportation phenomena as discussed above elucidate that if the configuration parameters of the serial-wedge-shaped channel are not designed properly, the lengthwise boundary of the junction may induce a severe pinning effect and cease the SDPT. Meanwhile, the two distinct motion statuses of droplets at the first junctions of channels with diverse w_1 are generated according to the results from the interplay between the driving forces (F_C and F_L) and the opposing forces (F_P and F_F). To ascertain how the configuration parameters of the channel influence the motion status of the droplet at the junction, which further influences the SDPT, we next utilized numerical simulation to model the transportation processes on different channels. Fig. 3(a) and (b) illustrate the simulation results of droplets on the serial-wedge-shaped channels with $\alpha = 4^\circ$, $w_1 = 0.4$ mm & 0.5 mm, and $w_2 = 1.0$ mm (the boundary of the channel was denoted by the black dash line). The separation of droplets into an anterior front and a posterior bulge can also

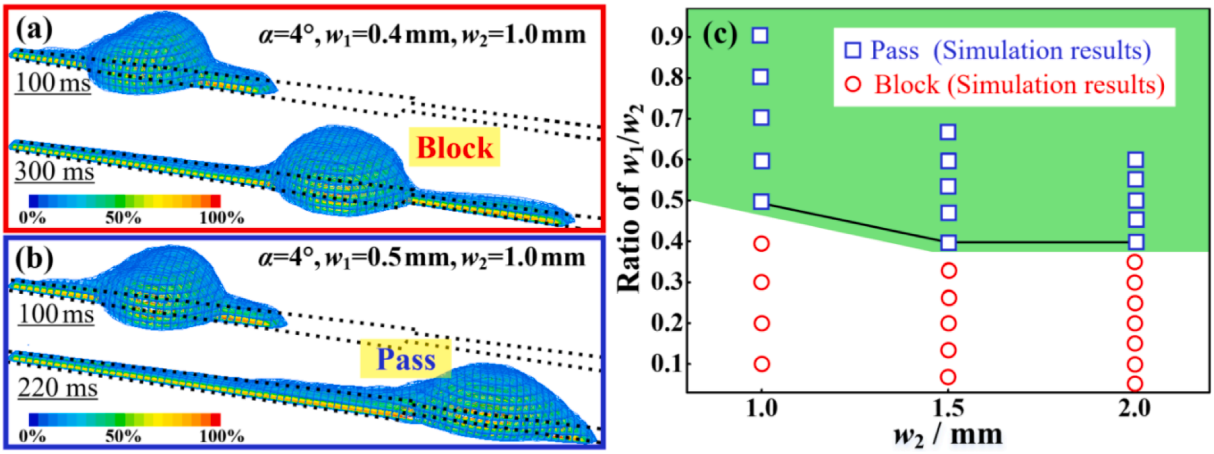

Fig. 3. Numerical simulation of the SDPT on the serial-wedge-shaped channels. (a, b) Transportation processes of droplets on the channels with $\alpha = 4^{\circ}$, $w_1 = 0.4$ mm & 0.5 mm, and $w_2 = 1.0$ mm. (c) Phase diagram showing motion statuses of droplets on channels with different configuration parameters.

be detected at 100 ms, which is in good agreement with the aforementioned experimental results. Then, the droplet exhibits block-status at the junction of the channel with $w_1 = 0.4$ mm at 300 ms, while exhibits pass-status on the channel with $w_1 = 0.5$ mm at 220 ms. Furthermore, using a similar simulation method, we obtained the motion statuses of droplets on the channels with $\alpha = 4^{\circ}$, and different w_1 and w_2. Fig. 3(c) is

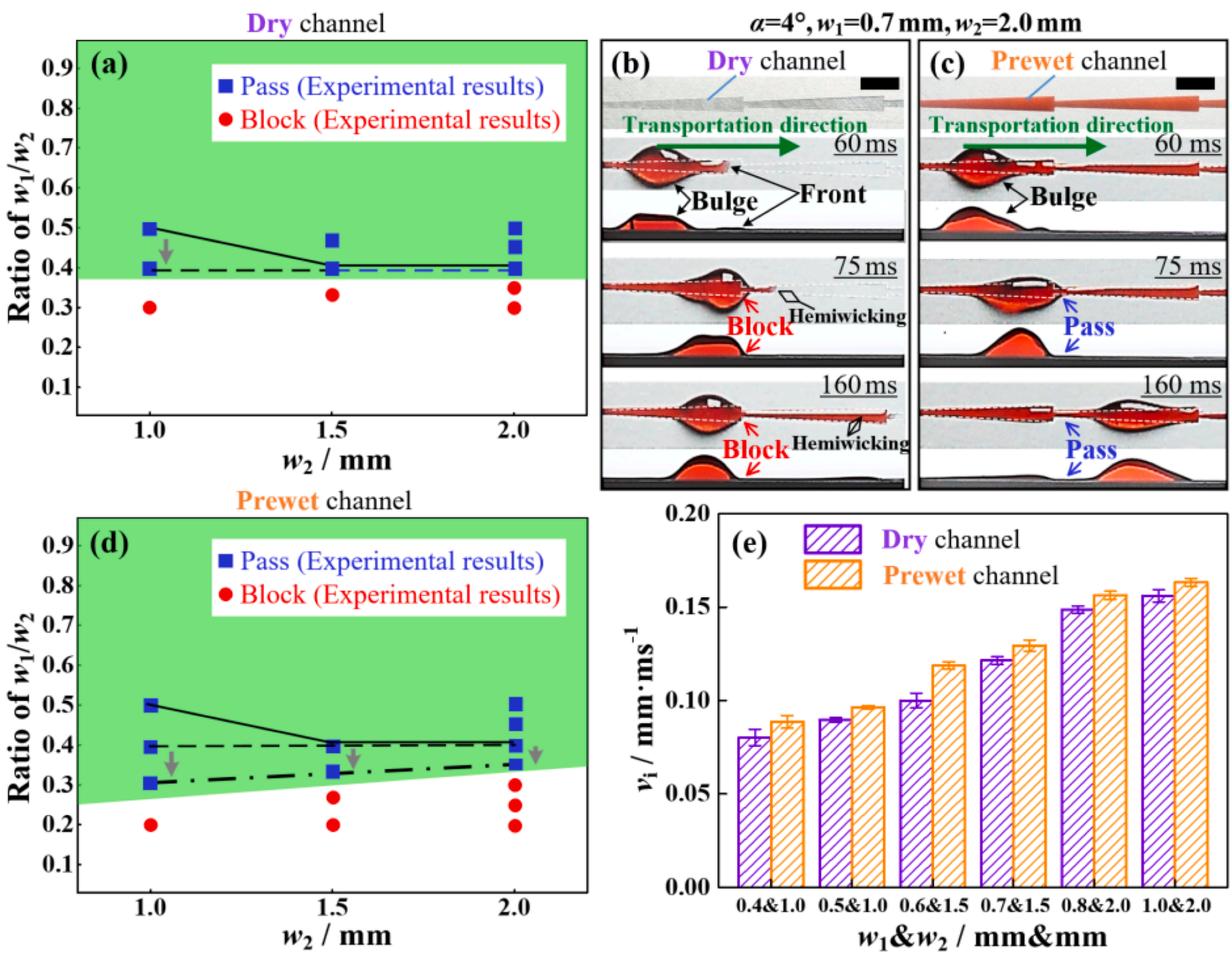

Fig. 4. Experimental verification of the SDPT on the serial-wedge-shaped channels. (a) Phase diagram showing motion statuses of droplets on dry channels with different configuration parameters. (b, c) Transportation processes of droplets on the dry/prewet channel with $\alpha = 4^{\circ}$, $w_1 = 0.7$ mm, and $w_2 = 2.0$ mm showing the block-status/pass-status. (d) Phase diagram showing motion statuses of droplets on prewet channels with different configuration parameters. (e) Comparison of transportation velocity of a droplet on the dry/prewet channels with different configuration parameters. Scale bars, (b, c): 2.0 mm.

the phase diagram plotted based on the simulation results, wherein the hollow blue squares and the hollow red circles represent the pass-status and the block-status of the droplet at the junction, respectively. In addition, the relationship between the critical ratio of w_1/w_2 and w_2 is obtained and the simulational critical curve is denoted by the solid line in Fig. 3(c). As can be seen, for $\alpha = 4^\circ$, the serial-wedge-shaped channels with $w_2 = 1.0$ mm & ratio of $w_1/w_2 \geq 0.5$ ($w_1 \geq 0.5$ mm), $w_2 = 1.5$ mm & ratio of $w_1/w_2 \geq 0.4$ ($w_1 \geq 0.6$ mm), and $w_2 = 2.0$ mm & ratio of $w_1/w_2 \geq 0.4$ ($w_1 \geq 0.8$ mm) can ensure the pass-status of droplet, which means that the channels with configuration parameters plotted in green background of phase diagram can realize the continuous SDPT. Based on the aforementioned force analysis and numerical simulation, it can be concluded that, for a serial-wedge-shaped channel with a certain α and a certain w_2, there is a critical narrow width w_{1c} corresponding to a critical pinning force from the junction F_{PJc}; when w_1 is larger than w_{1c}, the generated F_{PJ} will be smaller than F_{PJc}, which results in the fact that the driving forces acting on the droplet will be strong enough to overcome the opposing forces and ensure the continuous SDPT.

In what follows, we experimentally investigated the SDPT of water on the serial-wedge-shaped channels. Herein, to acquire the actual critical curve distinguishing the pass-status region and the block-status region in the phase diagram, a small number of channels ($\alpha = 4^\circ$, $w_2 = 1.0$ mm & 1.5 mm & 2.0 mm) with the ratio of w_1/w_2 ranging from 0.3 to 0.5 were prepared and used for water transportation according to the simulation results, which offer assistance to our experimental study. Fig. 4(a) shows the phase diagram plotting the experimental results of droplet motion statuses on the channels with different configuration parameters, wherein the pass-status is denoted by the solid blue square and the block-status is denoted by the solid red circle, respectively. Moreover, the actual critical curve is also acquired as indicated by the dash line shown in Fig. 4(a) and the channel with $w_2 = 1.0$ mm & ratio of $w_1/w_2 \geq 0.4$ ($w_1 \geq 0.4$ mm), $w_2 = 1.5$ mm & ratio of $w_1/w_2 \geq 0.4$ ($w_1 \geq$ 0.6 mm), and $w_2 = 2.0$ mm & ratio of $w_1/w_2 \geq 0.4$ ($w_1 \geq 0.8$ mm) can ensure the pass-status of droplet. Note that the only difference between the simulational critical curve and the actual critical curve is that the simulational critical ratio of w_1/w_2 for $w_1 = 1.0$ mm is 0.5, while the actual one is 0.4.

Strikingly, we found that the droplet motion status at the first junction of a serial-wedge-shaped channel with specific configuration parameters can be switched from block-status to pass-status conveniently by the altering external condition. As shown in Fig. 4(b), the droplet demonstrated block-status on the dry channel with $\alpha = 4^\circ$, $w_1 =$ 0.7 mm, and $w_2 = 2.0$ mm. However, for the same channel, after it was prewet by 10 μL water, the droplet demonstrated pass-status and a continuous SDPT could be realized as shown in Fig. 4(c). It is necessary to note that the channel could be filled with 10 μL water in the prewetting process because the channel depth was only $\sim$ 50 μm. In this way, a precovered water film was formed and the droplet could be supported at the top of the film during SDPT, resulting in a decrease of frictional force F_F because the three-phase (channel − water − air) contact line at the bottom of the droplet was switched to the two-phase (water–air) contact line [17,36]. Additionally, it is estimated that the precovered water film may also generate the increase of F_L, which will also improve F and subsequently engender the continuous SDPT. Then, the phase diagram of droplet motion statuses was replotted based on the experimental results of transportation on prewet channels as shown in Fig. 4(d). Compared with the phase diagram concerning the transportation on dry channels (Fig. 4(a)), the critical ratio of w_1/w_2 for $w_2 =$ 1.0 mm, 1.5 mm, and 2.0 mm are all lowered, which leads to the moving down of actual critical curve for prewet channels as denoted by a dot-dash line shown in Fig. 4(d). It is thus clear that the scale of configuration parameters engendering the continuous SDPT (plotted in the green background) can be enhanced by a prewetting process.

Apart from switching the motion status of the droplet, we found that the prewet channels can also enhance transportation velocity during SDPT. Herein, six channels with $\alpha = 4^\circ$ and different w_1&w_2 that can achieve the continuous SDPT under the dry condition were selected according to Fig. 4(a) for comparative experiments. When these channels were prewet by water, a higher transportation velocity of a droplet at a transportation duration of 150 ms could be observed on each channel as shown in Fig. 4(e), demonstrating an enhanced transportation capacity compared to the dry channels.

Additionally, the influence of α on the transportation velocity of the droplet was studied. A PSS possessing four serial-wedge-shaped channels with $\alpha = 3^\circ$ & 4° & 5° & 6°, $w_1 = 1.0$ mm, and $w_2 = 2.0$ mm embedded in a superhydrophobic panel were prepared on a square sample as shown in Fig. S5, wherein the starting points of these four channels were connected at the center of the sample. To illustrate the difference of droplet transportation velocities on the channels with diverse α, water droplets were dispensed dropwise on the connected region of the channels at a flux of $\sim$ 40 $\mu L \cdot s^{-1}$. In this way, the SDPT of water on the channels could be triggered simultaneously. As shown in Fig. 5(a), after 2 s of transportation, the channel with $\alpha = 5^\circ$ yielded the farthest transportation distance of $\sim$ 50 mm compared to $\alpha = 3^\circ$ at $\sim$ 37 mm, $\alpha = 4^\circ$ at $\sim$ 38 mm, and $\alpha = 6^\circ$ at $\sim$ 36 mm, respectively. The average transportation velocities v_a could be consequently calculated, which were 25.3 ± 1.2 $mm \cdot s^{-1}$ for $\alpha = 3^\circ$, 26.1 ± 1.3 $mm \cdot s^{-1}$ for $\alpha = 4^\circ$, 29.6 ± 1.2 $mm \cdot s^{-1}$ for $\alpha = 5^\circ$, and 22.8 ± 1.7 $mm \cdot s^{-1}$ for $\alpha = 6^\circ$, respectively, as shown in Fig. 5(b). Moreover, through single-factor experiments, we also found that the best configuration parameters of w_2 and w_1 for a serial-wedge-shaped channel to gain the highest transportation velocity are 2.0 mm and 1.2 mm, respectively, as shown in Fig. 5(c) and (d). Accordingly, the optimum configuration parameters to realize the fastest SDPT are $\alpha = 5^\circ$, $w_1 = 1.2$ mm, and $w_2 = 2.0$ mm, respectively, and the corresponding v_a is 30.4 ± 1.5 $mm \cdot s^{-1}$.

By taking advantage of the optimum configuration parameters mentioned above, the transportation capacity of the serial-wedge-shaped channels for continuous SDPT of water was further explored at a flux of $\sim$ 40 $\mu L \cdot s^{-1}$. As the schematics illustrated at the top of Fig. 5(e $\sim$ g), the PSSs possessing superhydrophilic channels with complicated configurations embedded in superhydrophobic panels are developed. These PSSs are composed of two parts: a channel for water transportation and a reservoir for water collection. Herein, a superhydrophilic reservoir is designed at the terminal point of each channel and utilized to collect water. Fig. 5(e) and (f) show that the continuous SDPT of water can be achieved on the horizontal long-distance straight channel with several right angles and the horizontal curving channel, respectively. Besides, the SDPT of water was also manifested on an inclined straight channel with a 3° tilt angle as shown in Fig. 5(g); under this circumstance, although gravity acts as the opposing force impeding the SDPT, water still overcomes gravity and can be successfully pumped up a ramp to an elevation of $\sim$ 4.5 mm.

Since the lengthwise boundary of the junction that is perpendicular to the transportation direction generally induces pinning effect to water and impedes SDPT, we then promoted an optimization strategy (the details are shown in Fig. S6) for the serial-wedge-shaped channel to adjust the configuration of the junction from an angular structure to a smooth structure, which is expected to improve droplet motion status at the junction and also enhance transportation velocity. Herein, the original channel ($\alpha = 5^\circ$, different w_1 and w_2) is denoted as optimized channel 0 (OC-0) and the optimized channels corresponding to 8 different optimization lengths l_O (from one-eighth to eight-eighths of the length between two junctions l_A, elucidated in Fig. S6) are denoted as optimized channel 1 $\sim$ optimized channel 8 (OC-1 $\sim$ OC-8), respectively. Thus, each optimized channel possesses its optimization scheme (optimization scheme 1 $\sim$ optimization scheme 8) which corresponds to a specific l_O.

In Fig. S7, we plotted the phase diagram of droplet motion statuses on the dry OC-0 with different configuration parameters based on experimental results. To evaluate the effect of optimization, transportation capacities of the dry OC-1 $\sim$ OC-8 were investigated experimentally and their phase diagrams of droplet motion statuses were

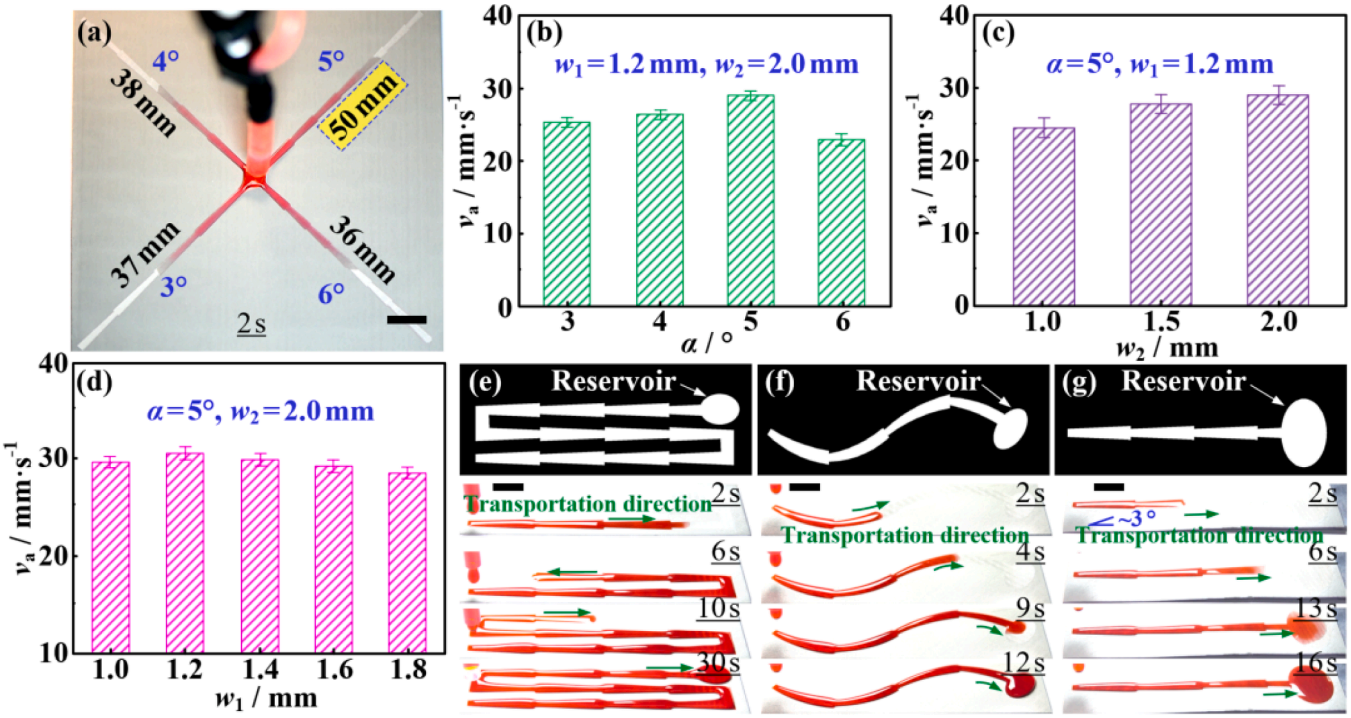

Fig. 5. Influence of different configuration parameters on transportation velocity of water and the SDPT of water on different PSSs. (a) Digital image of the SDPT on channels with $\alpha = 3^\circ$ & 4° & 5° & 6°, $w_1 = 1.0$ mm, and $w_2 = 2.0$ mm. (b ~ d) Influences of α, w_1 and w_2 on transportation velocity. (e ~ g) Schematics of the PSSs and digital images of SDPT on the horizontal long-distance straight channel, horizontal curving channel, and inclined straight channel. Scale bars, (a, e ~ g): 10 mm.

subsequently plotted in Fig. 6(a ~ h). Moreover, the upper and the lower dash lines illustrated in Fig. 6(a) are the actual critical curves distinguishing the pass-status region and the block-status region for the phase diagram of the dry OC-0 and OC-1, respectively. As can be seen, compared with the critical ratios of w_1/w_2 on OC-0 for ensuring pass-status, the ones on OC-1 (lower dash line) decreased from 0.4 to 0.3 for $w_2 = 1.0$ mm, from 0.33 to 0.27 for $w_2 = 1.5$ mm, and from 0.3 to 0.15 for $w_2 = 2.0$ mm, respectively. Therefore, after being subjected to optimization scheme 1 to adjust the configuration, the scale of configuration parameters ensuring pass-status of the droplet at the junction and engendering the continuous SDPT can be significantly enhanced.

Fig. 6(b ~ h) shows the phase diagrams of droplet motion statuses at the first junctions of dry OC-2 ~ OC-8, which is subjected to optimization scheme 2 ~ optimization scheme 8, respectively. For the OC-1 to OC-3, the scale of configuration parameters plotted in the green background that engenders continuous SDPT increases with l_O (from one-eighth to three-eighths of l_A) as shown in Fig. 6(a ~ c). Furthermore, for the OC-4 to OC-8 corresponding to l_O from three-eighths of l_A to eight-eighths of l_A, any configuration parameter plotted in the phase diagrams shown in Fig. 6(d ~ h) can ensure the pass-status and realize the continuous SDPT. It is speculated that the improvement of droplet motion statuses may be aroused by the smaller pinning effect from the optimized junctions of OC-1 ~ OC-8. In brief, applying the optimization strategy has a distinctive advantage in enlarging the parameters scale,

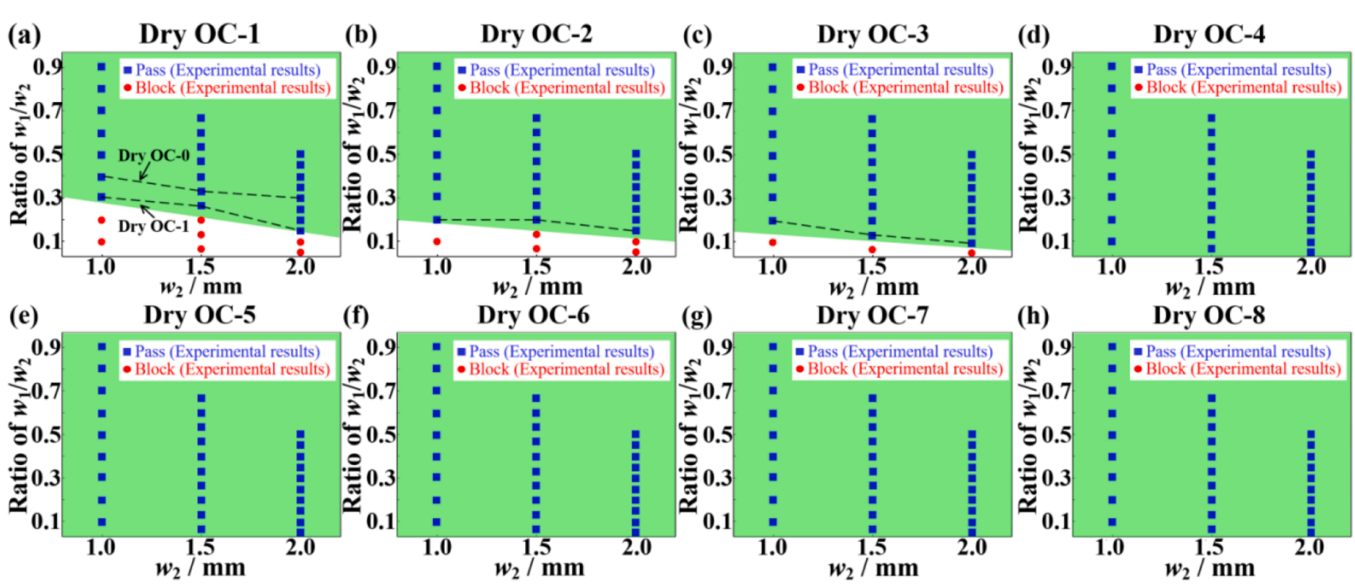

Fig. 6. Phase diagrams showing motion statuses of droplets on the dry optimized channels with $\alpha = 5^\circ$, and different w_1 and w_2. (a ~ h) OC-1 ~ OC-8.

which is beneficial to ensure the pass-status of the droplet at the junction and promote the continuous SDPT.

Investigation of the transportation velocity of the droplet on the optimized channels also helps evaluate the quality of different optimization schemes. For the serial-wedge-shaped channel with $\alpha = 5°$, $w_1 = 1.2$ mm, and $w_2 = 2.0$ mm, all its optimized channels (OC-1 ~ OC-8) can realize the continuous SDPT of water because the droplets demonstrate pass-status at the junctions according to Fig. 6(a ~ h). Schematics of the OC-0 ~ OC-8 are illustrated in Fig. 7(a), wherein l_A is 9.20 mm and l_O ranges from 0 mm to 9.20 mm. It can be detected that the angular junction of OC-0 is gradually adjusted into the smooth junction of OC-8 with the increase of l_O.

We next modeled the SDPT of a droplet on the OC-0 ~ OC-8, respectively. To calculate the simulative transportation velocities, a monitoring interface located at 26 mm from the starting point is set in each simulation model to record the passing time of water. Note that the length between the starting point and the first junction of each optimized channel is shorter than 26 mm. Fig. 7(b) and (c) show the SDPT of droplets on the OC-0 and OC-5, respectively, and the droplets arrive at the monitoring interfaces at different time. Based on the simulation results, average simulative transportation velocities of droplets v_{as} on the OC-0 ~ OC-8 were subsequently obtained. Fig. 7(d) elucidates that v_{as} first increases with the increase of l_O (0 mm for OC-0 ~ 5.75 mm for OC-5); after achieving the maximum v_{as} of ~ 51.7 mm·s^{-1} on the OC-5, v_{as} then decreases gradually (5.75 mm for OC-5 ~ 9.20 mm for OC-8). Moreover, all the v_{as} on the OC-1 ~ OC-8 are higher than that on the OC-0. Thereafter, experimental verifications were performed to verify the simulation results. Experimental transportation velocities v_{ae} are shown in Fig. 7(e) and the same variation trend of velocity on the optimized channels can also be observed, which is in good agreement with the variation trend of simulation results. Similarly, the maximum v_{ae} of 31.8 ± 0.7 mm·s^{-1} was obtained on the OC-5 compared to the minimum v_{ae} of 30.4 ± 1.5 mm·s^{-1} on the OC-0, revealing a 5 % improvement. The serial-wedge-shaped channel with an improved configuration revealing an enhanced transportation capacity is expected to be employed on water harvesting platforms and heat transfer equipment, which may increase water collection efficiency and heat transfer efficiency, respectively. It is supposed that the increase of v_{ae} with l_O (0 mm for OC-0 ~ 5.75 mm for OC-5) is generated because the optimized channel produces a smaller F_{PJ} and results in a larger F, while the major cause of the subsequent decrease of v_{ae} with l_O (5.75 mm for OC-5 ~ 9.20 mm for OC-8) is the decline of F_L as well as F owing to the optimized channel with a longer l_O losing its geometry gradient gradually.

4. Conclusion

In summary, under the inspiration of the dorsal integument of *P. cornutum*, we developed a straightforward and reliable approach to fabricate PSSs with superhydrophilic serial-wedge-shaped channels embedded in superhydrophobic panels *via* nanosecond laser ablation and FAS modification, and investigated the SDPT of water on the channels through numerical simulation and experimental verification. In particular, we carefully observed the motion statuses of droplets at the first junctions of the channels with different configuration parameters and found that a smaller pinning force from the junction with a shorter lengthwise boundary could ensure the pass-status of droplet for continuous SDPT. Furthermore, we manifested that transportation capacities of the channels could be enhanced by a prewetting process; compared with dry channels, the scale of configuration parameters engendering continuous SDPT on prewet channels could be increased and transportation velocities of droplets on the prewet channels could also be improved. In addition, we demonstrated that the fastest SDPT at ~ 30.4 mm·s^{-1} could be obtained on the channel with $\alpha = 5°$, $w_1 = 1.2$ mm, and $w_2 = 2.0$ mm. Continuous SDPT of water could be achieved conveniently on the horizontal long-distance straight channel, the horizontal curving channel, and the inclined straight channel with the above optimum configuration parameters. We then proposed an optimization strategy that can adjust the channel configurations to further enhance their transportation capacities by alleviating the pinning effect at the junctions; results show that the optimized channel under any optimization scheme reveals a higher v_a than the original channel and the highest v_a is ~ 31.8 mm·s^{-1}, revealing a 5 % improvement. From a broader perspective, the generality of our finding will open a new avenue for the design of next-generation high-performance fluid transportation systems.

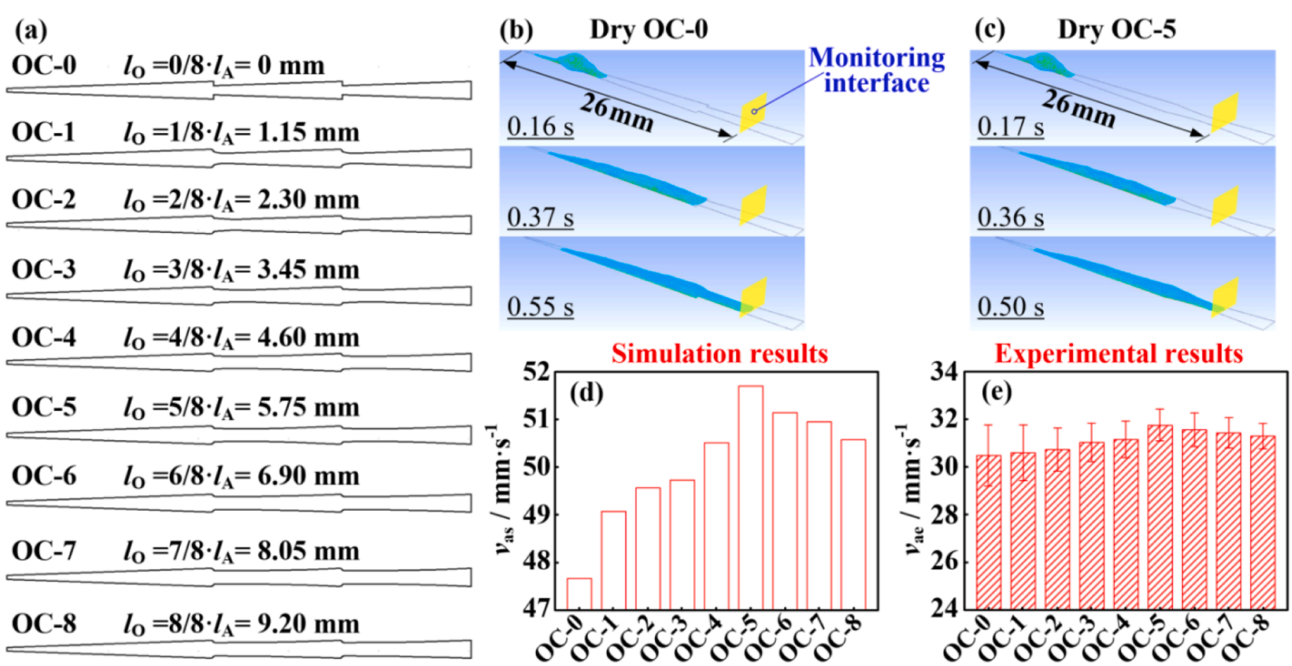

Fig. 7. SDPT of water on the optimized channels. (a) Schematics of the OC-0 ~ OC-8. (b, c) Transportation processes of droplets on OC-0 and OC-5 based on simulation results. (d, e) Transportation velocities of droplets on OC-0 ~ OC-8 based on simulation results and experimental results.

Declaration of Competing Interest

The authors declare that they have no known competing financial interests or personal relationships that could have appeared to influence the work reported in this paper.

Acknowledgments

This project was financially supported by the National Natural Science Foundation of China (NSFC, 52175380), the Dalian Youth Science and Technology Star (2018RQ01), the Fundamental Research Funds for the Central Universities (DUT21LAB120). We also thank Defeng Yan and Jinming Liu for some help in the part experiments.

Appendix A. Supplementary data

Supplementary data to this article can be found online at https://doi.org/10.1016/j.cej.2022.134568.

References

[1] H. Chen, P. Zhang, L. Zhang, H. Liu, Y. Jiang, D. Zhang, Z. Han, L. Jiang, Continuous Directional Water Transport on the Peristome Surface of Nepenthes Alata, Nature 532 (7597) (2016) 85–89.
[2] Y. Zheng, H. Bai, Z. Huang, X. Tian, F.-Q. Nie, Y. Zhao, J. Zhai, L. Jiang, Directional Water Collection on Wetted Spider Silk, Nature 463 (7281) (2010) 640–643.
[3] P. Comanns, G. Buchberger, A. Buchsbaum, R. Baumgartner, A. Kogler, S. Bauer, W. Baumgartner, Directional, Passive Liquid Transport: the Texas Horned Lizard as a Model for a Biomimetic 'Liquid Diode', J. R. Soc. Interface. 12 (2015) 20150415.
[4] J. Ju, H. Bai, Y. Zheng, T. Zhao, R. Fang, L. Jiang, A Multi-Structural and Multi-Functional Integrated Fog Collection System in Cactus, Nat. Commun. 3 (2012) 1–6.
[5] P. Ferraro, S. Coppola, S. Grilli, M. Paturzo, V. Vespini, Dispensing Nano-Pico Droplets and Liquid Patterning by Pyroelectrodynamic Shooting, Nat. Nanotechnol. 5 (6) (2010) 429–435.
[6] Q. Zhang, Y. Li, Y. Yan, X. Zhang, D. Tian, L. Jiang, Highly Flexible Monolayered Porous Membrane with Superhydrophilicity-Hydrophilicity for Unidirectional Liquid Penetration, ACS Nano 14 (6) (2020) 7287–7296.
[7] Y. Zhao, Y. Zhang, F. Li, Y. Bai, Y. Pan, J. Ma, S. Zhang, L. Shao, Ultra-Robust Superwetting Hierarchical Membranes Constructed by Coordination Complex Networks for Oily Water Treatment, J. Membr. Sci. 627 (2021) 119234.
[8] Y. Zhao, X. Yang, L. Yan, Y. Bai, S. Li, P. Sorokin, L. Shao, Biomimetic Nanoparticle-Engineered Superwettable Membranes for Efficient Oil/Water Separation, J. Membr. Sci. 618 (2021) 118525.
[9] W.-P. Huang, X. Chen, M.i. Hu, D.-F. Hu, J. Wang, H.-Y. Li, K.-F. Ren, J. Ji, Patterned Slippery Surface through Dynamically Controlling Surface Structures for Droplet Microarray, Chem. Mater. 31 (3) (2019) 834–841.
[10] U. Lee, J. Han, A. Elgowainy, M. Wang, Regional Water Consumption for Hydro and Thermal Electricity Generation in the United States, Appl. Energy 210 (2018) 661–672.
[11] T.P. Koukoravas, A. Ghosh, P.S. Mahapatra, R. Ganguly, C.M. Megaridis, Spatially-Selective Cooling by Liquid Jet Impinging Orthogonally on a Wettability-Patterned Surface, Int. J. Heat Mass Transf. 95 (2016) 142–152.
[12] Y. Li, L. He, X. Zhang, N. Zhang, D. Tian, External-Field-Induced Gradient Wetting for Controllable Liquid Transport: From Movement on the Surface to Penetration into the Surface, Adv. Mater. 29 (2017) 1703802.
[13] Y. Cui, D. Li, H. Bai, Bioinspired Smart Materials for Directional Liquid Transport, Ind. Eng. Chem. Res. 56 (17) (2017) 4887–4897.
[14] Y. Zheng, X. Gao, L. Jiang, Directional Adhesion of Superhydrophobic Butterfly Wings, Soft Matter. 3 (2) (2007) 178–182.
[15] M. Aliabadi, A. Zarkesh, M. Mandavinejad, Bioware Fog Collectors: the Texas Horned Lizard as a Model for a Biomimetic Fog-Harvesting, Mater. Res. Express 5 (2018) 115502.
[16] P. Comanns, C. Effertz, F. Hischen, K. Staudt, W. Boehme, W. Baumgartner, Moisture Harvesting and Water Transport through Specialized Micro-Structures on the Integument of Lizards, Beilstein J. Nanotechnol. 2 (2011) 204–214.
[17] H. Chen, T. Ran, Y. Gan, J. Zhou, Y.i. Zhang, L. Zhang, D. Zhang, L. Jiang, Ultrafast Water Harvesting and Transport in Hierarchical Microchannels, Nat. Mater. 17 (10) (2018) 935–942.
[18] J. Wang, S. Yi, Z. Yang, Y. Chen, L. Jiang, C.-P. Wong, Laser Direct Structuring of Bioinspired Spine with Backward Microbarbs and Hierarchical Microchannels for Ultrafast Water Transport and Efficient Fog Harvesting, ACS Appl. Mater. Interfaces 12 (18) (2020) 21080–21087.
[19] Q. Wang, B. Su, H. Liu, L. Jiang, Chinese Brushes: Controllable Liquid Transfer in Ratchet Conical Hairs, Adv. Mater. 26 (2014) 4889–4894.
[20] Y. Chen, K. Li, S. Zhang, L. Qin, S. Deng, L. Ge, L.-P. Xu, L. Ma, S. Wang, X. Zhang, Bioinspired Superwettable Microspine Chips with Directional Droplet Transportation for Biosensing, ACS Nano 14 (4) (2020) 4654–4661.
[21] K. Li, J. Ju, Z. Xue, J. Ma, L. Feng, S. Gao, L. Jiang, Structured Cone Arrays for Continuous and Effective Collection of Micron-Sized Oil Droplets from Water, Nat. Commun. 4 (2013) 1–7.
[22] J. Li, Y. Song, H. Zheng, S. Feng, W. Xu, Z. Wang, Designing Biomimetic Liquid Diodes, Soft Matter. 15 (9) (2019) 1902–1915.
[23] X. Yang, J. Song, J. Liu, X. Liu, Z. Jin, A Twice Electrochemical Etching Method to Fabricate Superhydrophobic-Superhydrophilic Patterns for Biomimetic Fog Harvest, Sci. Rep. 7 (2017) 1–12.
[24] J. Song, F. Guan, W. Pan, Z. Liu, J. Sun, S. Ling, X. Deng, Y. Sun, Droplet-Based Self-Propelled Miniboat, Adv. Func. Mater. 30 (2020) 1910778.
[25] H. Zheng, S. Huang, J. Liu, F. Chen, X. Yang, X. Liu, J. Sun, W. Xu, V Vein-Like Directional Transport Platform of Water on Open Aluminium Substrate, Micro, Nano Lett. 11 (2016) 269–272.
[26] A. Ghosh, R. Ganguly, T.M. Schutzius, C.M. Megaridis, Wettability Patterning for High-Rate, Pumpless Fluid Transport on Open, Non-Planar Microfluidic Platforms, Lab Chip 14 (9) (2014) 1538–1550.
[27] J. Song, Z. Liu, X. Wang, H. Liu, Y. Lu, X.u. Deng, C.J. Carmalt, I.P. Parkin, High-Efficiency Bubble Transportation in an Aqueous Environment on a Serial Wedge-Shaped Wettability Pattern, J. Mater. Chem. A 7 (22) (2019) 13567–13576.
[28] J. Li, X. Zhou, J. Li, L. Che, J. Yao, G. McHale, M.K. Chaudhury, Z. Wang, Topological liquid diode, Sci. Adv. 3 (10) (2017), https://doi.org/10.1126/sciadv.aao3530.
[29] Q. Zhang, L. He, X. Zhang, D. Tian, L. Jiang, Switchable Direction of Liquid Transport via an Anisotropic Microarray Surface and Thermal Stimuli, ACS Nano 14 (2) (2020) 1436–1444.
[30] K. Hou, X. Li, Q. Li, X. Chen, Tunable Wetting Patterns on Superhydrophilic/Superhydrophobic Hybrid Surfaces for Enhanced Dew-Harvesting Efficacy, Adv. Mater. Interfaces 7 (2020) 1901683.
[31] Z. Wang, Y. Lu, S. Huang, S. Yin, F. Chen, Bamboo-Joint-Like Platforms for Fast, Long-Distance, Directional, and Spontaneous Transport of Fluids, Biomicrofluidics 14 (2020) 034105.
[32] D. Shi, Y. Chen, X. Chen, X. Chen, J. Gao, Y. He, C.-P. Wong, Ladderlike Tapered Pillars Enabling Spontaneous and Consecutive Liquid Transport, ACS Appl. Mater. Interfaces 10 (40) (2018) 34735–34743.
[33] S. Feng, Q. Wang, Y. Xing, Y. Hou, Y. Zheng, Continuous Directional Water Transport on Integrating Tapered Surfaces, Adv. Mater. Interfaces 7 (2020) 2000081.
[34] X. Yang, K. Zhuang, Y. Lu, X. Wang, Creation of Topological Ultraslippery Surfaces for Droplet Motion Control, ACS Nano 15 (2) (2021) 2589–2599.
[35] H. Ma, M. Cao, C. Zhang, Z. Bei, K. Li, C. Yu, L. Jiang, Directional and Continuous Transport of Gas Bubbles on Superaerophilic Geometry-Gradient Surfaces in Aqueous Environments, Adv. Func. Mater. 28 (2018) 1705091.
[36] Z. Liu, H. Zhang, Y. Han, L. Huang, Y. Chen, J. Liu, X. Wang, X. Liu, S. Ling, Superaerophilic Wedge-Shaped Channels with Precovered Air Film for Efficient Subaqueous Bubbles/Jet Transportation and Continuous Oxygen Supplementation, ACS Appl. Mater. Interfaces 11 (26) (2019) 23808–23814.